

TESTING COSMOLOGICAL MODELS BY GRAVITATIONAL LENSING:

I. Method and First Applications

Joachim Wambsganss
Astrophysikalisches Institut Potsdam, 14482 Potsdam, Germany
jwambsganss@aip.de

Renyue Cen and Jeremiah P. Ostriker
Princeton University Observatory, Princeton, NJ 08544
cen, jpo@astro.princeton.edu

ABSTRACT

Gravitational lensing directly measures mass density fluctuations along the lines of sight to very distant objects. No assumptions need to be made concerning bias, the ratio of fluctuations in galaxy density to mass density. Hence, lensing is a very useful tool to study the universe at low to moderate redshifts.

We describe in detail a new method to trace light rays from redshift zero through three dimensional mass distribution to high redshift. As an example, this method is applied here to a standard cold dark matter universe. We obtain a variety of results, some of them statistical in nature, others from rather detailed case studies of individual “lines of sight”. Among the former are the frequency of multiply imaged quasars, the distribution of separation of the multiple quasars, and the redshift distribution of lenses: all that as a function of quasar redshift. We find effects from very weak lensing to highly magnified multiple images of high redshift objects, which, for extended background sources, (i.e. galaxies), range from slight deformations of the shapes through tangentially aligned arclets up to giant luminous arcs.

Different cosmological models differ, increasingly with redshift, in their predictions for the mass (thus gravitational potential) distributions. Our ultimate goal is to apply this method to a number of cosmogonic models and to eliminate some models whose gravitational lensing properties are inconsistent with those observed.

Subject headings: gravitational lensing, dark matter, cosmology, methods: numerical

1. Introduction

Each specific model for the development of cosmogonic structure (e.g. the hot dark matter [HDM] or cold dark matter [CDM] scenarios) has one free parameter, the amplitude of the density power spectrum. In the light of the COBE observations (Smoot et al. 1992; Gorski et al. 1994), it occurs, for the first time, that this parameter is fixed ($\pm 12\%$) by the determination on the $5^\circ - 10^\circ$ scale in the linear regime. With its amplitude fixed, a secure determination of the potential fluctuation on any other scale provides a test for a particular cosmological model. Any single conflict between the theory and reality can falsify the former. The most leverage is obtained for tests which are made on angular scales as far away as possible from the COBE measurements. But they should not be so small as to be greatly influenced by the difficulty inherent in modeling the physics of the gaseous, baryonic components ($\leq 10kpc$). Thus, critical tests are best made on scales $0.01Mpc < r < 1Mpc$. Gravitational lensing measures *directly* the fluctuations in the gravitational potential along random lines of sight to distant objects. In contrast, the conventional tools for comparing cosmogonic theories with observations rely on either galaxy density or galaxy velocity information, both of which unavoidably suffer from the uncertain situations with regard to density or velocity bias of galaxies over the underlying mass distribution, hampering our attempts to understand the more “fundamental” question concerning the mass evolution and distribution. Hence gravitational lensing provides a powerful, independent test of cosmogonic models, because of its unique ability to directly measure the gravitational potential fluctuations. The sampled properties of cosmic structure on certain scales are also more “fair” than other conventional measures owing to the fact that lines of sight to distant objects are *random* with regard to the foreground matter distribution.

We present here a method to determine gravitational lensing effects for realistic mass distributions from the weak to the strong lensing regime. First, we fill the universe “densely” with adjacent mass cubes, taken from cosmological simulations, along the line of sight, where inside each cube the matter is projected onto the middle plane. Then, we study the lensing properties of the intervening matter by “shooting” light rays through the lens (mass) planes representing matter distributions along redshifts (cf. Figure 1 for a schematic version of our actual scheme [which uses of order 100 lens planes]). The gravitational lens effects of many lens planes have been studied by several authors in the past (e.g., Kochanek & Apostolakis 1988; Schneider & Weiss 1988a,b; Jaroszyński 1989, 1991; Jaroszyński et al. 1990; Lee & Paczyński 1990; Babul & Lee 1991; Bartelmann & Schneider 1991). These authors have typically used point lenses or isothermal spheres which were randomly distributed on individual lens planes. The number of lens planes used ranges from 2 to 32. Most of these studies involved the regime of weak lensing, i.e. slight effects on the magnification of sources, but not multiple imaging. Rauch (1991) studied the microlensing

effect of three-dimensionally distributed point lenses on high redshift supernovae. A complementary approach to the one described here, a semi-analytical method using the Press-Schechter formalism was first used by Narayan and White (1987), and more recently applied by Kochanek (1995) to various cosmological models.

A very preliminary attack on the problem of studying the lensing properties of different cosmological models has been presented by Cen et al. (1994, hereafter CGOT). In that work no ray tracing was done. Rather it was simply checked whether or not mass accumulations were greater than the critical level (cf. Turner, Ostriker & Gott 1984, henceforth TOG) at which multiple imaging will occur. The mathematical and physical treatment here is far superior to that adopted in CGOT; the essential conclusions for the standard CDM scenario, however, are unchanged. Some of these conclusions have already been presented in Wambsganss et al. (1995). Here we provide the mathematical basis of that method as well as some tests of the method.

We use cosmological simulations for the standard COBE-normalized $\Omega = 1$, CDM universe as an example to illustrate the method. A first report on the results has been published elsewhere (Wambsganss et al. 1995). In principle, mass distributions from any cosmological model can be treated with this method. The ultimate goal of this project is to provide a quantitative comparison of the lensing properties of different cosmological models (e.g., CDM with $\Omega = 1$; low density (open) CDM models; mixed dark matter [MDM] models; flat models with a cosmological constant; isocurvature models etc) with observations. For example, we anticipate that different cosmological models, which are typically tuned to give approximately the right properties when being compared with our local universe at redshift $z = 0$, will show different lensing properties because they reach the final state ($z = 0$) from quite different paths. Thus, the typical lens will appear at different redshifts in different models. For example, in MDM models, where structure forms late, the lenses will have small redshift, but in isocurvature models, where the first structures form shortly after recombination, the average lens redshift will be much larger.

For many questions (e.g. the fraction of multiply imaged quasars as a function of angular separation, magnification ratio, redshift) one needs a large number of simulations with different realizations of the matter distribution, in order to give quantitative answers on a good statistical basis. For other applications, e.g. detailed studies of lensing by clusters of galaxies and the effects of chance alignments with foreground or background matter, a specific realization must be studied in detail.

While it is in principle possible to simulate, numerically in one simulation, the entire path from observer to source (very large simulations with elongated geometry have been done; e.g., Park & Gott 1991), technical limitations preclude this at the present time. For

now we perform many independent simulations for different volumes along the line of sight (since repeated structures are obviously to be avoided). We have developed an approximate technique for this which we term the “convolution method”. Physically it consists of assuming that separate pieces of an inhomogeneous universe act as if they were part of an homogeneous universe of the same mean density as themselves. Details of the method, which is an improved version over that applied in CGOT, are presented in the Appendix, as well as detailed checks which indicate the accuracy of the approximations involved.

Although we think this convolution technique describes the properties accurately enough on the scales in which we are interested, we hope in the future to be able to avoid this step and be able to use simulations that have a large enough dynamic range to cover a representative part of the universe and have high enough resolution in order to represent the potential wells of galaxies, groups and clusters appropriately. The analytical techniques presented in this paper for the determination of the lens properties are independent of the details of the method for computing the evolution. We will use the same ray tracing method when later we utilize higher resolution numerical evolution techniques which do not depend on the convolution method.

The rest of the paper is organized as follows. The ray-shooting technique is described and discussed in detail in Section 2. As a result of this ray-shooting, we obtain a mapping of the rays from the image plane (sky plane) to the source plane. With this mapping it is possible to determine the magnification distribution of background sources, the fraction of the source plane that is multiply imaged, the positions and shapes as well as the topology of the caustics and the corresponding critical lines (Section 3). For a set of given source positions and shapes in the source plane at a given redshift, we determine and analyze the corresponding image configurations as they would appear in the sky, as is shown in Sections 4 and 5. Finally in Section 6 we give a short summary and describe the planned applications and the types of predictions we will be able to make for the different cosmological models.

2. Multiplane Lens Equation, Ray Shooting, Tests

In Schneider, Ehlers and Falco (1992, subsequently SEF) a whole chapter deals with the theory of multiple light deflection, i.e. gravitational lensing by more than one plane. We refer the interested reader to this text book for details. Here we just describe the multiplane lens equation as we use it:

$$\begin{pmatrix} y_1 \\ y_2 \end{pmatrix} = \vec{y} = \vec{x} - \sum_{i=1}^N \frac{D_{is}}{D_s} \vec{\alpha}_i(\vec{x}) = \begin{bmatrix} a_{11}(\vec{x}) & a_{21}(\vec{x}) \\ a_{12}(\vec{x}) & a_{22}(\vec{x}) \end{bmatrix} \begin{pmatrix} x_1 \\ x_2 \end{pmatrix} = A(\vec{x})\vec{x}. \quad (1)$$

Here \vec{x} is the position vector of a light ray in the first lens plane (or equivalently in the image/sky plane); \vec{y} is its corresponding position in the source plane; $\vec{\alpha}_i$ is the (two dimensional) deflection angle in lens plane # i ; D_s and D_{is} are the angular diameter distances between observer and source plane and between i th lens plane and source plane, respectively. The lens planes are labelled from 1 through N in order of increasing redshift.

The part of the equation that we are essentially interested in is $\vec{y} = A(\vec{x})\vec{x}$; it describes just the mapping between the image/sky plane and the source plane. The relation between the positions \vec{x} in the image/sky plane and \vec{y} in the source plane is given by $A(\vec{x})$, the Jacobian matrix of the mapping. In the case of multiple lens planes the Jacobian

$$A(\vec{x}) \equiv \frac{\partial \vec{y}}{\partial \vec{x}}, \quad A_{ij} \equiv \frac{\partial y_i}{\partial x_j}, \quad (2)$$

does not have all the nice properties it has in the single lens plane case, in particular it is not symmetric any more in the general case: $a_{12} \neq a_{21}$. Furthermore it is not curl-free: $\text{curl} A \neq 0$. Many other properties, however, are still valid. The magnification of a certain image at position \vec{x} is given as

$$\mu(\vec{x}) = [\det A(\vec{x})]^{-1} = [a_{11}(\vec{x})a_{22}(\vec{x}) - a_{12}(\vec{x})a_{21}(\vec{x})]^{-1}. \quad (3)$$

We will see in later sections that other combinations of the components of $\det A(\vec{x})$ represent useful quantities as well. The effective surface mass density κ (which is basically the sum of the physical surface mass densities of the individual lens planes, weighted by the corresponding ratios between the angular diameter distances) for any position \vec{x} in the sky plane is given as

$$\kappa(\vec{x}) = 1 - 0.5 [a_{11}(\vec{x}) + a_{22}(\vec{x})]. \quad (4)$$

Similarly, the components of the shear $\vec{\gamma}(\vec{x}) = [\gamma_1(\vec{x}), \gamma_2(\vec{x})]$ are

$$\gamma_1(\vec{x}) = -0.5 [a_{11}(\vec{x}) - a_{22}(\vec{x})]; \quad (5a)$$

$$\gamma_2(\vec{x}) = -0.5 [a_{12}(\vec{x}) + a_{21}(\vec{x})]. \quad (5b)$$

In order to “shoot” a light ray i through a single lens plane, what must be done is to determine the deflection angle $\vec{\alpha}_i$ of this ray due to all matter in this lens plane. For a number of n point lenses this is just a summation of the deflection angle by each point lens j :

$$\vec{\alpha}_i = \sum_{j=1}^n \alpha_{ji} = \frac{4G}{c^2} \sum_{j=1}^n M_j \frac{\vec{r}_{ij}}{r_{ij}^2}. \quad (6)$$

Here G and c are the gravitational constant and the speed of light, respectively, M_j is the mass of point lens j , r_{ij} is the projected (vector) distance between the positions of light ray

i and point lens j , and r_{ij} is its absolute value, $r_{ij} = \sqrt{(x_i - x_j)^2 + (y_i - y_j)^2}$; here (x_i, y_i) is the position of ray i , and (x_j, y_j) is the position of lens j .

The straightforward determination of one deflection angle takes about ten floating point operations. As a lens plane, we consider a two-dimensional distribution of matter that is given in a grid; for the examples here we will always use a regular matter grid with 500^2 positions (in subsequent work we will increase the resolution to 800^2 positions; in principle this can be increased to any desired resolution, depending on the desired purpose). This is the projection of the three-dimensional matter distribution inside a cube with comoving side length $L = 5h^{-1}Mpc$ (where $h = H_0/100$ is the Hubble constant divided by 100) onto one of the three faces of the cube. We treat this matter distribution as 250,000 point lenses, or more accurately, as “smeared out” in matter or lens pixels, i.e. in a square region of comoving $10h^{-1}kpc$ at a side. We must determine the deflection angle at least at as many positions as there are lens pixels, i.e. at least on a 500^2 grid (again, this is the resolution we use for the examples here; this can be changed to whatever ray density is appropriate to the problem at hand). Because we will use of order 100 lens planes, the total number of mathematical operations for a direct determination of the deflection angle amounts to about $10 \times 500^2 \times 500^2 \times 100 \approx O(10^{14})$ floating point operations. This is non-trivial, even for fast computers.

In order to speed up the calculation we determine the deflection angle in each lens plane with a hierarchical tree code in two dimensions, as described in Wambsganss (1990). The idea is to group together lenses that are far away from the light ray, and treat these “cells” (whose sizes increase with the distance to the ray) as pseudo-lenses. Nearby lenses are treated individually, lenses at intermediate distances to the light ray are grouped into small cells of a few lenses, and those lenses very far away from the light ray considered, are in cells containing up to a few thousand lenses. This tree code treatment speeds up the determination of the deflection angle by a large factor. The number of lenses and pseudo-lenses necessary for an accurate determination of the deflection angle in one plane is of order 100 (rather than 250,000 for the direct determination). There is some overhead, namely the determination of the tree structure for each ray, i.e. the configuration of which lenses have to be treated directly and which ones are to be put in cells of different sizes. However, this is done just once, and used again in all subsequent planes, since the relative positions of the lenses are exactly the same. The cost of this additional calculation is negligible compared to that of a direct determination of the deflection angles.

In its simplest application the tree code assumes that all matter inside a cell is located at its center of mass. We do, however, use higher order multipoles of the mass distribution in order to increase the accuracy (cf. Wambsganss 1990). For the actual calculations we

use multipoles up to order 6. In Figure 2 we show the deviation of the deflection angle determined with this tree-code method from the directly determined, i.e. accurate deflection angle: $(\alpha_{direct} - \alpha_{tree})$ as a function of α_{direct} in arbitrary units (the top row indicates the x-component, the bottom row the y-component). The panels correspond to determinations of α_{tree} including multipoles of different order; they represent: all matter in center of mass, i.e. only monopole term (leftmost column), monopole term plus quadrupole moments (2nd column), monopole term plus all multipoles up to order 4 (3rd column), and monopole term plus all multipoles up to order 6 (rightmost column). In the actual calculation of the deflection angle we use multipoles up to order 6, corresponding to the rightmost panel. It can be seen that for this case the largest deviation between the two methods of determining the deflection angle is of order 2×10^{-3} , with the rms deviation quite a bit smaller. This seems to be a good enough approximation for our purposes.

For point lenses the deflection angle formally diverges when the distance between light ray and lens position becomes zero, $r_{ij} \rightarrow 0$. However, in our case this is an artificial divergence, because the underlying mass distribution is smooth, we only approximate it by a large number of point lenses. In order to avoid this artificial divergence, we always determine the deflection angle at the points directly in the center between four lens positions so that nearest neighbor effects cancel. That means, for each lens plane we determine the deflection angles for a regular grid of “test-rays”. But, since the real positions of the light rays are offset from the positions of these “test-rays”, for which we determined the deflection angles, we calculate the actual deflection angles of the rays that are followed through the planes using a bicubic interpolation between the four test-rays surrounding the real ray position. In this way we obtain a smooth two-dimensional field of deflection angles for each lens plane, as is to be expected for a continuous matter distribution.

The angular size of the (square) bundle of light rays that we consider is determined by the angular size of the highest redshift lens plane that we use. As an example, the angular size of a cube with comoving size $L = 5h^{-1}Mpc$ at a redshift $z = 3$ is about $\beta \approx 350$ arcsec for a standard CDM universe. The (average) angular size of the field of rays is fixed, it is the same for all lens planes; however, as the physical size of the underlying cosmological cubes is expanding with decreasing redshift, the angular size of the lens planes increases rapidly with decreasing redshift. This means that the field of real-rays intercepts only a small part of the lens plane for small redshifts (cf. Figure 1). This effect is reflected in the matter distribution inside the field of view: for low redshift lens planes, one lens-pixel (which has fixed comoving size) covers quite a large angular region.

The matter distribution of each lens plane inside the field of rays is shown in Figure 3a for a particular line of sight: dark (light) gray means high (low) surface mass density (in

grams per cm^2). From top left to bottom right you see the matter inside the beam for 60 different lens redshifts, starting with $z \approx 0$ and increasing to $z \approx 3.0$. For the low redshift planes one can easily identify the pixel size of the matter distribution, because there one matter pixel (physical size $5 h^{-1} \text{ Mpc} / (1+z)/500 = 10h^{-1}(1+z)^{-1}\text{kpc}$) corresponds to many tens of arcsecs. In Figure 3b the integrated matter distribution up to a redshift $z \approx 3.0$ is shown. This is the “physical” sum, i.e. in units of mass per physical area. This map could be converted into a map of light, if one assumes, e.g., a constant mass-to-light ratio and weights the individual lens planes by the inverse of the (luminosity) distance. If one compares Figures 3a and 3b, it is quite obvious that the total surface mass density is dominated by a few planes along the line of sight. In general, lensing is a very convergent process: it is not due to the sum of a large number of weak lensing events; rather it is due to the occasional passage of a light ray past a large mass concentration. This fact makes the requirements for statistical validation of our results especially stringent. Many independent realizations of the universe must be made and many lines of sight examined before one can have confidence (by examination of convergence) that the derived statistical results are robust (i.e. the statistically averaged results become independent of the number of realizations studied).

For each lens plane the critical surface mass density Σ_{crit} necessary for multiple imaging can be calculated (cf. SEF):

$$\Sigma_{crit} = \frac{c^2}{4\pi G} \frac{D_s}{D_i D_{is}}. \quad (7)$$

Comparing the surface mass density in each matter pixel (m, n) with this number identifies the regions that should produce multiple images of a background source:

$$\kappa_{m,n} = \Sigma_{m,n} / \Sigma_{crit} = \Sigma_{m,n} * \frac{4\pi G}{c^2} \frac{D_i D_{is}}{D_s},$$

where $\Sigma_{m,n}$ is the physical surface mass density in pixel (m, n) , and $\kappa_{m,n}$ is its normalized surface mass density. When $\kappa_{m,n} > 1$, then multiple lensing occurs. We note, however, that overdensity in a single plane is a sufficient but not necessary condition of multiple imaging; chance alignments of two or more individually subcritical but collective supercritical regions can produce multiple images as well as slightly underdense regions in combination with a sufficiently large value of shear. A comparison of such regions with the actual location of multiple images serves as a good check of the whole method.

For each complete run of the light rays through all the lens planes, the positions of the light rays in the image/sky plane and the corresponding positions in the source plane are stored. In subsequent sections we will describe how the matter distribution is obtained in each lens plane, and how we analyze the mapping of light rays through essentially a realistic

3-dimensional matter distribution. But first we like to add a few paragraphs discussing the issue of numerical resolution, and describing an additional test of our method.

Many authors have studied magnification cross sections and caustic structures of various lens models. To name just a few: Blandford & Kochanek (1987) and Kochanek & Blandford (1987) studied magnification cross sections and probability distributions for isolated elliptical potentials; Hinshaw & Krauss (1987) determined the lensing probabilities for isothermal spheres with finite cores; Wallington & Narayan (1993) investigated the influence of the core radius on the imaging properties of elliptical lenses; Kovner (1987a,b) looked into “marginal” lenses; Kassiola & Kovner (1993) compared the lensing properties of elliptical mass distributions with elliptical potentials. Most of these authors studied idealized lens models in great detail. In order to get a good representation of, e.g., the magnification probability of a certain elliptical lens, one needs a grid of rays with good coverage of the source plane, in particular of the multiply imaged region (of order 1000^2 rays).

We have a very different objective here, we want to study large scale statistical lensing properties of the matter rather than to model and understand individual lenses in great detail. Therefore our resolution is very different from those examples mentioned above, i.e. we have many fewer rays covering the caustics region of our multiply imaging lenses than they have. This is due to the different questions we try to answer. Nevertheless, we like to know how well the lensing properties are reproduced in the high magnification regions. Therefore we compare the lensing properties of ideal elliptical lenses as obtained with our method to the high resolution results obtained by others.

First we describe here briefly how we determine the magnification: We evaluate the magnification in a regular grid in the source plane, as is explained in more detail in Chapter 4. This is done by using the differential deflection properties of the four rays closest to the grid position to be evaluated. Subsequently we interpolate two-dimensionally, to determine the value at the desired position. This way we do get a moderate resolution though certainly not a perfect coverage of the multiply imaged region: a region with size about $(350 \text{ arcsec})^2$ is covered by about 500^2 resolution elements in the examples here. However, we would like to emphasize that the resolution is not hardwired in this method. It can and will be increased with the availability of faster computers with more memory or for the investigation of specific problems.

Below we present a test of the accuracy of the magnification distribution obtained by our method. For that purpose we use elliptical lenses with different parameters (ellipticity, core radius, velocity dispersion). We test the accuracy of our method by using elliptical lenses as described by Wallington & Narayan (1993, henceforth WN93). We run tests with

a single lens plane populated by an isolated elliptical lens with various values of ellipticity, velocity dispersion and core radius. The results of these tests show that the qualitative lensing properties (the caustic geometry, the evolution of the caustic/critical line structure with increasing core radius, as shown in Fig.1 of WN93) are well reproduced.

We also did a detailed quantitative comparison of the magnification distributions produced by the various elliptical lenses with the cross sections presented by WN93 (see their Fig.3). We determined the cross sections for lensing of elliptical lenses with nine different velocity dispersions ranging from $\sigma_v = 370$ km/sec to 1000 km/sec. The ellipticities were chosen between 0.0 and 0.2 and we varied the core radii from 10% to 100% of the Einstein radius of a corresponding circular symmetric isothermal sphere. We compared the cross sections for magnifications larger than 2, 4, 8, 16, 32, ... with the values obtained by WN93. For each “lens” as specified by the parameter set of velocity dispersion, ellipticity, and core radius, we run 10 different realisations (in terms of angle relative to the coordinate axes and position of center of lens). Here is the summary of the comparison of our results with those of WN93, for three values of the velocity dispersion $\sigma_{v1} = 370$ km/sec, $\sigma_{v2} = 630$ km/sec, $\sigma_{v3} = 1000$ km/sec, all with ellipticity $\epsilon = 0.2$, and with various core radii. The distributions $\sigma(> \mu)$ for magnifications $\mu = 2, 4$ and 8 agreed within about 15% or better for all three values of σ_v . For $\mu = 16$ the deviations were still moderate for the two higher σ_v -values (23% and 11%), whereas it was worse than that for the low velocity dispersion σ_{v1} . Even for $\mu = 32$, the deviation was only 30% for σ_{v3} , but quite large for the two lower values.

This indicates that the cross sections of gravitational lenses with velocity dispersions at or below 1000 km/sec are relatively well represented in the low and intermediate magnification regime. At high magnifications they are not very accurately represented in our simulations with the given resolution. However, the fluctuations in the cross sections are mostly of statistical nature (the high magnification regions are covered only by a small number of resolution elements), as we could infer from comparisons among the 10 realisations we had used for each parameter set. In the applications of our method, there are always *many* lenses in each of our “lines-of sight”, and since we will use 100 or more different lines of sight for our statistical analyses, the deviations relative to the WN93 values will get (much) smaller, again, due to the decreasing statistical noise. Hence we do get a fair enough representation for the low and moderately high magnification regime. As we are interested mainly in the global statistical properties rather than the local ones, this test shows that our approach is justified.

3. Determination of the Underlying Matter Distributions

The matter evolution used in this paper is simulated by a Particle-Mesh (PM) N-body code (Cen 1992). But a direct, brute force calculation with such a code is unable to cover the dynamic range needed: a ratio of cluster-cluster separation ($100h^{-1}\text{Mpc}$) to the lensing scale of arcseconds ($10h^{-1}\text{kpc}$) translates to 10^{12} mesh points, which is far beyond the current generation of supercomputers. In order to overcome this problem a novel scheme involving convolution of a small scale simulation box (which provides good resolution) with a large scale simulation box (which provides good statistical information concerning clusters) was developed (CGOT). We basically use their scheme of convolving two box sizes, but we add a few essential improvements. Our scheme is described in detail in the Appendix.

The three dimensional matter distribution from these calculations is given for any cosmological time as three two-dimensional projections onto the x-y, y-z, and x-z-planes, with an effective resolution of comoving $10h^{-1}\text{kpc}$, which is necessary in order to study the lens effects on small angular scales of approximately 5 arcsec. Were we to wish to study still smaller scales, hydrodynamic simulations (cf. e.g. Cen 1992; Katz, Hernquist, & Weinberg 1993; Navarro, Frenk & White 1994; Summers, Davis & Evrard 1995; Steinmetz & Müller 1994) would be required since the baryonic component begins to dominate over the dark matter component within 10 kpc. The essence of the convolution method is to note that small regions of given over (or under) density act for most processes as if they were in homogeneous universes of larger (or smaller) mean density. For details and checks of the method see the Appendix.

For a typical lensing simulation a few hundred lens planes with size $L = 5h^{-1}\text{Mpc}$ are required. Ideally one would like to have as many independent cosmological sequences as lens planes used. This is not achievable for reasons of limited CPU time. But neither is it really necessary. The reason is that for most of the planes only a small fraction of the matter distribution is “illuminated” by the bundle of light rays (see Figure 1). In practice, we use ten independent evolutionary runs. For a given lens redshift the particular run to be used for this particular lens plane is chosen randomly, as is the projection to be used out of the three possible ones, as is the location and orientation of the square region that is “illuminated” by the rays.

The computing time for such a lensing simulation is directly proportional to the number of lens planes used. Most of the lens planes have densities that are below the average density of the universe (because a few have a high overdensity), some are almost completely empty. These lens planes contribute very little to the deflection angle. We did some experiments in bunching together a couple of lens planes at adjacent redshifts, that

means adding up the matter distributions, and treating the combined matter distribution as a single “pseudo”-plane. We found that for a grouping of about 10 real lens planes into one pseudo lens plane, the results (see next sections) are indistinguishable from treating all the lens planes individually. So we concluded by running the simulations with only 60 pseudo-planes (up to a redshift of $z_S = 3$), where each one represents a grouping of 10 real planes. That means, in fact that one of our pseudo-lens planes represents a rectangular parallelepiped of size $5h^{-1} \times 5h^{-1} \times 50h^{-1}\text{Mpc}^3$.

4. Magnification Pattern and Magnification Distribution

In Figure 4a (COLOR PLATE) a two-dimensional magnification pattern is shown, representing the magnification as a function of source position at a redshift of $z_S = 3$ for one particular lensing run of our example cosmology, a standard CDM model with $\Omega = 1$ and $\sigma_8 = 1.05$. The magnification is shown as a function of position in the source plane. By definition, the average magnification is $\langle \mu \rangle = 1.0$, or $\langle \Delta m \rangle = -2.5 \log \langle \mu \rangle = 0$, i.e. equal to the case where all the matter is smoothly distributed. Whenever we use “magnification” (or demagnification) subsequently, we mean magnification (or demagnification) relative to a situation in which all matter is smoothly distributed.

The magnification as a function of position in the source plane is shown color-coded in Figure 4a: it increases from blue through green and red to yellow. The border line between green and red corresponds roughly to the average magnification $\mu = 1.0$. Green regions have magnifications slightly less than one (i.e., they are slightly de-magnified, compared to a universe in which all matter were smoothly distributed). Red color indicates magnifications of up to one magnitude, yellow magnification by more than one magnitude. Note that there is quite a large region that gets demagnified by a small amount, and a few relatively small spots that get quite high magnification.

Such a magnification pattern in the source plane is similar to the magnification patterns used in microlensing simulations at much smaller angular scales (e.g., Wambsganss, Paczyński & Schneider 1990). One difference between the magnification patterns used here and those used in microlensing is that there one is interested in the change of magnification as a function of time (due to the relative motion of observer, lens and source), whereas here we only study the changes in the magnification as a function of position. Another difference is that here we find caustics (and multiple images) only in rare cases, because we basically study the lens properties of a more or less smooth mass distribution; in such a situation, the surface mass density must be above the critical value, in order to produce caustics. In (quasar) microlensing, ensembles of point lenses are studied, which always produce many

(micro-)images and, correspondingly, many caustics.

An example of a two dimensional distribution $\mu(\vec{x})$ of magnification in the *image/sky plane* (cf. eq(3)) is shown in Figure 4b (COLOR PLATE). It shows the magnification that an image seen at this particular position in the sky would have. The color assignment is the same as for Figure 4a, except that here there are locations with black color, that means formally very high negative values of the magnification. The boundaries between regions with high positive and those with high negative magnifications (transitions from yellow to black) are easy to identify. These are the critical lines.

This image plane magnification distribution is quite similar, but not identical, to the magnification distribution in the source plane shown in Figure 4a. The differences are most obvious for highly magnified positions that correspond to multiple images. Whereas in Figure 4a (magnification pattern in the *source plane*), the *total* magnification of all images corresponding to this source positions is displayed, in Figure 4b the *sky plane* magnification of the different images at the corresponding positions are shown. From the distribution in Figure 4b alone, however, it is not obvious, which images belong to the same source position.

In Figure 5 the magnification probability distribution for the underlying cosmological model is shown. The top panel shows the differential distribution, the bottom panel the integrated one. It shows the relative frequency $f(\mu)$ of magnification μ , sampled in ten equally spaced logarithmic intervals per decade. (In contrast to most other Figures, this one shows the result of all 100 different realizations, rather than that of an “example” line-of-sight only). In the differential distribution (top panel) there is a strong peak just left of magnification $\mu = 1.0$, and a power law tail ($f(\mu) \propto \mu^{-2}$) to high magnifications (the same power law dependence as found in TOG for point lenses and in subsequent work for more realistic matter distributions) until the probability drops to zero due to the finite resolution. The thin solid line in Figure 5 indicates the magnification distribution for single image cases only, whereas the dotted line is the one for multiple images only (the bold line is the sum of the two). Because of the rareness of very high magnifications, the high magnification end naturally is quite noisy.

The magnification distribution in Figure 5 can be interpreted as the “transfer function” of the matter in the universe (i.e., for this particular cosmological model). In other words: Any intrinsic luminosity function of, say, quasars, will be folded with this magnification distribution, and what we see as the observed quasar luminosity function is the convolution of the intrinsic luminosity function with this “transfer function” of the universe (Vietri & Ostriker 1983). In principle one can determine the intrinsic quasar luminosity function for a given cosmological model, once the observed luminosity function and the transfer function

of this cosmological model are known (Ostriker & Vietri 1986). In practice this will turn out to be non-trivial, mainly because the observed luminosity function of quasars is not well known (Boyle, Shanks & Peterson 1988).

The effect of this transfer function is even more obvious when applied to a population of perfect “standard candles” at high redshift: for a given source redshift, the luminosity function (originally a delta function in such a case) will be broadened to exactly the shape $f(\mu)$ indicated by the curve in the top part of Figure 5. The slope of this magnification probability function for gravitational lensing is known analytically in the limit of very high magnifications (TOG; Schneider 1987; Blandford & Narayan 1986) and should therefore be independent of the cosmological model. However, in the intermediate range from small to moderate magnifications, different cosmological models produce different magnification probability distributions.

5. Caustics, Critical Lines, Multiple Images

As described in Section 2, the positions of all rays in the image plane and in the source plane are stored for each lensing run. Therefore it is straightforward to determine characteristics of the mapping $\vec{y} = A\vec{x}$ between the positions in the image plane \vec{x} and those in the source plane \vec{y} (see SEF, Chapter 5).

Of particular interest are the points in the image plane \vec{x} at which the Jacobian determinant $\det A(\vec{x})$ changes its sign (in the previous section it was pointed out that these points can be seen in Figure 4b as the locations where the color changes from yellow to black). By definition these are the *critical lines*. In Figure 6a the critical lines are plotted for this particular line of sight. Mapping these critical lines onto the source plane results in the *caustics*. These are shown in Figure 6b. Comparing Figure 6a and 6b, it is not too difficult to find out which caustic belongs to which critical line.

The shapes of the critical lines and of the caustics found in these lensing simulations are quite irregular, they are certainly different from the symmetric shapes that are obtained for simple models of lenses, e.g. singular isothermal sphere plus external shear or elliptic potentials (e.g., Blandford & Kochanek 1987; Kormann, Schneider & Bartelmann 1994). The reason is simply that the mass distributions we use are not at all symmetric, but rather representing the irregular “real” distribution of matter in the universe.

Whenever the source position is inside such a closed caustics line, a pair of new (usually highly magnified) images emerges. When the source is outside, but near a caustic, one highly magnified image is resulting. In Figure 7 various image configurations are shown that

are produced by the caustic structure in the top right part of Figure 4a/6b. They indicate the variety of image shapes and morphologies that can be produced by this particular caustic structure. It ranges from a very stretched (and highly magnified) single image at the top left through elongated and aligned double and triple images of similar magnification through cases with faint central (radial) images. For comparison, the shape and size of a unlensed source is indicated at the bottom right corner of the bottom right panel.

One can look at these image configurations from two different viewpoints: if the source is extended (e.g., a distant galaxy), then Figure 7 shows the highly extended images that could be observed: giant arcs, arclets, tangentially aligned images. On the other hand, if the source is an unresolved quasar, then the area of the images reflects the magnification of the two or more quasars that are seen. The separation between the “centers of light” would be the distance between the multiple images. For comparison, in the lower right corner an unlensed source is shown, which represents magnification $\mu = 1.0$.

6. Giant Arcs, Arclets, Tangentially Aligned Galaxies, and Shear Maps

In this section we show the effects of gravitational lensing due to our three dimensional ray tracing on various ensembles of sources. In the left column of Figure 8 we show four different fields of sources: a regular grid of circular sources, randomly distributed circular sources, a regular grid of elliptical sources (with fixed ellipticity and random position angle) and randomly distributed elliptical sources with fixed ellipticity. The diameter of the circular sources shown here is about 3 arcsec. At the corresponding right-hand side the resulting image configurations are shown: this is what a telescope would see if a galaxy distribution at a redshift of $z_S = 1$ like that at the left side were seen through the matter distribution in front of it. The size of an image reflects the magnification, since surface brightness is conserved by gravitational lensing: the area of the images, divided by the area of the corresponding source, is the magnification of this particular image. Since all source sizes and shapes are identical in one panel, the relative areas of the images reflect the relative magnifications. In the panels with a regular grid of source positions, it is very obvious, from the deviations of the chains of galaxies from straight lines, where the largest matter concentrations exist along the line of sight (cf. with the map of the matter in Figure 3b).

Since all the sources have identical intrinsic sizes and shapes in each panel (circular or constant ellipticity), each deviation from that shape on the right hand side is lens-induced. One can see a large variety of lens-induced image shapes: slight ellipses from circular sources, small arcs, “straight arcs”, giant arcs, big blobs, and more complicated image

structures. Perhaps most obvious is the tendency of “tangentially aligned” (roughly) elliptical images, whose major axes are about perpendicular to the radius vector from the center of the mass concentration.

In Figure 9 the lensing effect of our example line of sight is shown for three different source redshifts: the left columns from top to bottom show three sets of circular sources with random positions at source redshifts $z_S = 1, 2, 3$. The second column shows the respective image configurations that one would see in the sky, if seen through the deflecting matter between source plane and observer. In the lowest row, the three source populations are superimposed, with the different redshifts indicated by three different gray scales.

In Section 2 we described how one can obtain the surface mass density κ (cf. eq. (4)) along the line of sight, as measured by the light rays. In Figure 4c (COLOR PLATE) we show the distribution of the effective surface mass density κ for our example field of view. The highest density clumps are easily identifiable with the highest magnification regions in Figures 4a and 4b. It is also quite obvious, how the magnification $\mu(\vec{x})$ (Figure 4b) follows the surface mass density distribution very closely (Figure 4c) in the low magnification regime. This indicates that it is the convergence, the matter inside the beam, that is mainly responsible for the magnification, and not so much the shear field from outside the beam.

For each of our artificial lines of sight, we can obtain the distribution of the shear fields as shown in eq. (5) in Section 2. For our example line of sight, this shear distribution $\vec{\gamma}(\vec{x})$ is shown for a source redshift of $z_S = 1.0$ in Figure 4d (COLOR PLATE). The length of the straight lines is proportional to the absolute value of the shear, and the direction represents the direction of the shear. It is quite obvious that the big lump of matter in the top right part produces the strongest shear, the lines clearly indicate the tangential alignment expected for galaxies that are behind such a cluster of galaxies. Similar shear distributions have recently been obtained observationally by various groups who study the distribution of shear in fields around rich clusters of galaxies (e.g., Bonnet et al. 1993) or in “empty” fields (Mould et al. 1994). Observationally, the shear fields are obtained by averaging the ellipticities of galaxies in small fields of a few tens of arcseconds. The idea is that this averaging should cancel the intrinsic distribution of position angles, and as a net effect just show the effective shear produced by the gravitational lens effect of the foreground matter.

7. Summary and Outlook

We have described a method to determine the lensing properties of a three dimensional, fully nonlinear distribution of matter, obtained from cosmological simulations. We explain

the techniques we use to calculate the light deflection by a large number of lenses in many lens planes. The simulations produce maps of the magnification in the source and image plane. We can study the caustics and critical lines for each matter realization individually, or in a statistical way for a large number of realizations. Here one particular “line of sight” with the matter distribution from a standard CDM model with $\Omega = 1$ and $\sigma_8 = 1.05$ is used, as an example, to illustrate diagnostic power of the applications. It is straightforward to apply this method to other cosmological models, and we plan to do so with significantly higher resolutions in both cosmological simulations and ray-tracing method. There are numerous possible applications of this ray shooting technique. Just to mention a few, which we plan to address in the future:

- 1) Study of frequency, geometry, magnification ratio, and separation of multiple images. What fraction of quasars is multiply imaged? How many double, triple, quadruple images do we obtain (for given observational limits of spatial resolution and dynamic range)?
- 2) Study of the distribution of magnification of certain classes of objects (galaxies, quasars); this can be done separately for single images and multiple image cases, or for both combined, addressing question like “are there many highly magnified quasars that are single (rather than multiply imaged)?”. Another straightforward application is a quantitative study of the dispersion effect of lensing on standard candles at moderate redshifts (i.e. on supernovae of type 1).
- 3) Study of correlations between single/multiple quasars and strong (“visible”) mass concentrations at or near the line of sight (which may affect the issues of dark lenses and/or quasar-galaxy-associations)
- 4) Study of effects of chance alignments of dense matter clumps along the line of sight: how accurate are the mass determinations which assume that all matter responsible for the lensing is in a single plane?
- 5) Study of the shear distribution/tangentially aligned galaxies around (rich) clusters and in “empty” fields. What is the average or rms-shear value in random lines of sight?
- 6) Use techniques of reconstructing mass profiles of galaxy clusters from weak lensing (Kaiser & Squires 1993), and compare the reconstructed mass profile with the actual one. Are there any systematic effects due to foreground and background matter?
- 7) Compare the frequency and properties of arcs and “straight arcs” produced by extreme lensing in clusters with that seen in the real world.
- 8) Study of the effects of three dimensional lensing on the cosmic microwave background.

Most of the points above can be investigated for sources at different redshifts. We know that the expected and computable gravitational lensing properties of the different models, that have been proposed for the growth of structure in the universe, will vary greatly from model to model. Thus a quantitative comparison between observed and expected lensing properties should offer great power in selecting among the competing models, and ideally allow us to eliminate models which fail to correspond to reality. Even at present the strongest constraints on the size of the cosmological constant are derived from lensing statistics (Fukugita & Turner 1991; Kochanek 1992; Maoz & Rix 1993, Kochanek 1995) In a recent application of the method described here, we (Wambsganss et al. 1995) found that the standard CDM model predicts far more large splitting multiple quasars than are observed. It will be very interesting to see if other models such as mixed dark matter, CDM+ Λ or open models can survive this gravitational lensing test.

It is a pleasure to thank Michal Jaroszyński, Avi Loeb, Jordi Miralda-Escudé, Peter Schneider, and Ed Turner for many useful discussions at various stages of this project. We also want to thank an anonymous referee for his constructive criticism of the first version of the manuscript, which significantly improved the quality of this paper.

Appendix: Description of the Convolution Technique

Here we describe the “convolution method”, which is used to compensate the lack of sufficient spatial dynamic range in the N-body simulations. As stated earlier in the main body of this paper, for gravitational lensing applications one must have enough scale-resolving power to reach scales which are interesting and accessible to observations (\sim arcsecond). But it is not possible at the same time, in a single simulation, to reach the other end of the spectrum, the large scale waves of the universe, to have a fair sample of the relevant cosmic systems, which are clusters of galaxies in this case. A minimal desired dynamic range will be a few times the ratio of cluster separation ($\sim 50h^{-1}\text{Mpc}$) to cluster core size ($50h^{-1}\text{kpc}$), i.e., a few thousand, which was not achievable at the time when the simulations used in this paper were computed.

As an alternative to the brute-force approach, we made two kinds of simulations: one with box size $L = 5h^{-1}\text{Mpc}$ (Box-S hereafter) and resolution of $10h^{-1}\text{kpc}$, the other with box size $L = 400h^{-1}\text{Mpc}$ (Box-L hereafter) and resolution of $0.8h^{-1}\text{Mpc}$ (both simulations use 500^3 cells with a PM N-body code). In computations of both boxes (S,L) we assume periodic boundary conditions. That is we assume that both boxes have the same mean density as the universe at any given redshift. For the large box that is a good approximation

since the amplitudes of waves on scales larger than $400h^{-1}\text{Mpc}$ are quite small at $z = 0$ and even smaller at the redshifts relevant for lensing. But for the small box, this assumption is poor. The nonlinear scale at $z = 0$ is approximately $8h^{-1}\text{Mpc}$ so, in the L box we will find $5h^{-1}\text{Mpc}$ subboxes at a variety of over and under densities. Then using this distribution we convolve Box-S (which has small scale resolution) with Box-L (which has large scale power), details of which are described below. We also note that, at the time this paper is being written, we are using new N-body techniques to make simulations which can cover this needed range directly. We note that the gravitational ray-tracing method presented in the paper is independent of the convolution method described here.

Before a step-by-step description of the convolution method, it is useful to define a few quantities. The actual over- or under-density of a particular plane, $R = \Sigma / \langle \Sigma \rangle$, drawn from the density distribution $f(R)$ on the scale of Box-S (5^3h^{-3}Mpc^3), which is computed from Box-L (containing 512,000 subboxes each of which is a 5^3h^{-3}Mpc^3 cube). R is the ratio of the density in the Box-S to the mean cosmic density. The projection of the matter in a Box-S onto one of the three orthogonal planes makes a surface mass density screen called $\Sigma_1(\vec{x})$. We now detail steps to do the convolution.

1) We first choose R randomly from $f(R)$.

2) Then a mosaic square region, $\Sigma_2(\vec{x})$, consisting of $N^2 \Sigma_1(\vec{x})$ screens, where $N = 2, 3, 4, \dots$, is set up. The number of repetition screens, N , in each dimension on the projection plane is determined by R such that the shrunk $\Sigma_4(\vec{x})$ (when $R > 1$, see step 4 below) still has a comoving length larger than $1.5 \times (5h^{-1}\text{Mpc})$ to prevent situations of no defined densities from happening, when rays shoot outside the original region.

3) From Σ_2 we obtain a new screen called, $\Sigma_3(\vec{x})$ equal to $\Sigma_2^{R^{0.07}}(\vec{x})$, where the power operation operates on each individual cell of screen Σ_2 . This step is to mimic the evolution of regions with different densities and the value 0.07 is empirically determined using simulations. This step does not, to first order, change the overall density but it increases the contrast (for $R > 1$). Since $R^{0.07}$ is always very close to unity, this step affect the results very mildly.

4) Next, we rescale each of the two dimensions of the screen $\Sigma_3(\vec{x})$ by $R^{-1/3}$. This involves resampling the surface mass onto a smaller (or larger) grid for $R > 1$ ($R < 1$), increasing (decreasing) the surface density by $R^{2/3}$, resulting in a new screen, $\Sigma_4(\vec{x}) = \text{SCALE}(\Sigma_3(\vec{x}))$. This step is to take account of the fact that high density regions should have been compressed to smaller comoving regions during their evolution.

5) The density in each of the new pixels of Σ_4 is multiplied by $R^{1/3}$ to take into account the effect that the line of sight dimension is also reduced, yielding $\Sigma_5 = R^{1/3}\Sigma_4$.

6) Randomly choose an origin and randomly rotate screen Σ_5 to get, by bilinear interpolation, a new screen Σ_6 with the original comoving pixel size ($10h^{-1}\text{kpc}$).

7) Finally, renormalize Σ_6 such that $\langle \Sigma_6 \rangle = R \times \langle \Sigma_1 \rangle$, which will be the end product of this scheme. The renormalization factor R is typically very close to unity.

In Figure 10 we illustrate this convolution. The four panels correspond to the original surface mass density distribution Σ_1 (top left), a part of the shrunk or expanded distribution Σ_5 (top right), the full Σ_5 (bottom left), and the final rotated and normalized distribution Σ_6 (bottom right). In Figure 10a this is shown for a factor $R = 1.6$ (over dense), in Figure 10b for $R = 0.625$ (under dense)

This convolution method is tested against a high resolution P³M simulation (Bertschinger 1995) where the boxsize is $100h^{-1}\text{Mpc}$ and therefore it contains large scale power. Of course, this P³M simulation does not reach the resolution of $10h^{-1}\text{kpc}$ on the small scale end, so we can only make comparisons in the overlapping region. Figure 11 shows the surface density distributions on a cell of area $125 \times 125h^{-2}\text{kpc}^2$ with depth of $100h^{-1}\text{Mpc}$ using our convolution method (solid histogram) and from direct calculation using Bertschinger’s simulation (dotted histogram). The agreement is satisfactory.

REFERENCES

- Babul, A. & Lee, M.H. 1991, MNRAS 250,407
- Bartelmann, M. & Schneider, P. 1991, A&A 248,353.
- Bertschinger, E. 1995, private communication
- Blandford, R.D. & Kochanek, C.S. 1987 ApJ 321, 658
- Blandford, R.D., Narayan, R. 1986, ApJ 310, 568
- Bonnet, H., Fort, B., Kneib, J.-P., Mellier, Y., Soucail, G., 1993, A & A 280, L7
- Boyle, B.J., Shanks, T , & Peterson, B.A. 1988, *ASP Conf. Ser.: “The evolution of optically selected QSOs”* **2**, 1
- Cen R. 1992, ApJS, 78, 341
- Cen, R., Gott III, J.R., Ostriker, J.P., Turner, E.L. 1994, ApJ 423, 1 (CGOT)
- Fukugita, M. & Turner, E.L. 1991, MNRAS 253,99
- Gorski et al. 1994, ApJ 430, 89

- Hinshaw, G., Krauss, L.M. 1987, ApJ 320, 468
- Jaroszyński, M. 1989, Acta Astr., 39, 301
- Jaroszyński, M. 1991, MNRAS 249,430
- Jaroszyński, M., Park, C., Paczynski, B. & Gott, J.R. 1990, ApJ 365, 22
- Kaiser, N., & Squires, G. 1993, ApJ 404, 441
- Kassiola, A., Kovner, I. 1993, ApJ 417, 450
- Katz, N., Hernquist, L., & Weinberg, D.H 1993, ApJ, 399, L109
- Kochanek, C.S. 1992 ApJ 384, 1
- Kochanek, C.S. 1995 ApJ 453, 545
- Kochanek, C.S. & Apostolakis, J. 1988 MNRAS 235, 1073
- Kochanek, C.S. & Blandford, R.D. 1987, ApJ 321, 676
- Kormann, R., Schneider, P., Bartelmann, M. 1994, A & A 284, 285
- Kovner, I. 1987a, ApJ 321, 686
- Kovner, I. 1987b, Nature 325, 507
- Lee, M.H. & Paczyński, B. 1990, ApJ 357,32
- Maoz, D. & Rix H.-W. 1993 ApJ 416, 425
- Mould, J., Blandford, R., Villumsen, J., Brainerd, T., Smail,I. 1994, ApJ 271, 31
- Navarro, J..F, Frenk, C., and White, S.D.M. 1994, MNRAS, 267, L1
- Narayan, R., & White, S.D.M. 1987, MNRAS, 231, 97p
- Ostriker, J.P. & Vietri, M. 1986, ApJ 300, 68
- Park, C.B., & Gott, J.R., III 1991, MNRAS, 249, 288
- Rauch, K.P. 1991, ApJ 374, 83
- Schneider, P. 1987, A & A 183, 189
- Schneider, P. & Weiss, A. 1988a, ApJ 327,526
- Schneider, P. & Weiss, A. 1988b, ApJ 330,1
- Schneider, P., Ehlers, J., & Falco, E.E., *Gravitational Lensing* (Springer Verlag, Berlin, 1992) (SEF)
- Smoot, G.F., et al. 1992, ApJ(Letters), 396, L1
- Steinmetz, M, and Müller, E. 1994, A & A 281, 97

- Summers, F., Davis, M., and Evrard, A. 1995, ApJ, 454, 1
- Turner, E.L., Ostriker, J.P., and Gott, J.R. III 1984 ApJ 284, 1 (TOG)
- Vietri, M. & Ostriker, J.P. 1983, ApJ 267, 488
- Wallington, S., & Narayan, R. 1993, ApJ 403, 517 (WN93)
- Wambsganss, J. 1990 Ph.D. Thesis, Munich University; available as MPA report #550
- Wambsganss, J., Paczyński, B., & Schneider, P. 1990 ApJ 358, L33
- Wambsganss, J., Cen, R., Ostriker, J. P., & Turner, E. L. 1995, Science 268, 274

FIGURE CAPTIONS

Figure 1 Schematic depiction of the bundle of light rays with fixed opening angle traversing many planes with constant comoving (but increasing physical) side length. For simplicity we show only three lens planes, in fact we use of order 100 individual planes. The observer is at the left hand side, the source plane is at the right hand side. Redshifts of the lens planes are increasing from left to right, (i.e., $0 < z_i < z_j < z_k < z_S$). The bundle of light rays “illuminates” a small fraction of the lens planes at low redshift. This fraction increases with redshift to almost one at the highest lens redshift.

Figure 2 Displayed is the effect of increasing the accuracy of the hierarchical tree code for the determination of the deflection angle by using multipoles of higher order. The top (bottom) row deals with the x-(y-)component of the deflection angle. The difference between direct determination and tree-code determination is shown versus the direct determination (in arbitrary units). In the leftmost column the tree code uses just the monopole term, i.e. it assumes all the matter is at the location of the center of mass of each cell. The accuracy of the angle determination in this case is about 1 %. In the next columns the same is shown for a tree code including quadrupole moment (column 2) and tree code with all moments up to order 4 (column 3). In the right most column all multipole moments up to order 6 are included in the determination of the deflection angle. The maximum deviation in the last panel is clearly better than 0.1 %. All our lensing calculations are done with this accuracy.

Figure 3 The matter distribution in physical units (grams per cm^2) inside the beam of rays is shown. Dark color indicates high values of the surface mass density. Figure 3a: 60

panels contain the matter distribution of individually treated lens planes. The “first” plane is top left (lowest redshift), with redshift increasing to the right. The highest redshift plane is the last one in the bottom row at $z = 3$. In Figure 3b this matter integrated along the line of sight up to a redshift $z = 3$ is displayed.

Figure 4a Magnification pattern of one particular “line of sight” through the universe (the same as portrayed in Figure 3). This is a two dimensional map of the magnification as a function of position in the *source* plane at $z_S = 3$. The color indicates the *total* magnification of all images for a particular source position: it increases from blue through green and red to yellow. The transition between green and red marks roughly the average magnification. For the strong lens in the top right part the caustics are identifiable as sharp yellow lines, indicating very high magnification. The sidelength of this and all the other maps is 343 arcsec, comparable to the HST WFPC side length of 160 arcsec.

Figure 4b Magnification map in the *image/sky* plane. Here the magnification of each image appearing at a certain position in the sky is indicated. The low and intermediate magnification regions are very similar to those in the map shown in Figure 4a. At the high magnification end there are obvious differences: here each image of a multiply imaged source would appear at a different position. Note the transitions from bright yellow to black: Here the magnification changes from very high positive values to (formally) very high negative values. That means this boundary marks the “critical lines” which separate multiple images with positive and negative parity.

Figure 4c Map of effective surface mass density κ or convergence along the line of sight. This distribution is quite similar to the matter integrated along the line of sight, as shown in Figure 3b. However, here the matter is “weighted” by the angular diameter distances.

Figure 4d Shear map for a source plane at $z_S = 1$, due to the foreground mass distribution in the field of view. The length of the lines indicates the relative strength of the shear, the angles of the lines show the direction of the shear. The regions of strong shear are easily recognized as those with the highest mass concentrations (cf. Figures 3b, Figures 4a/b/c).

Figure 5 Magnification distribution from 100 different realizations (i.e., about 2.5×10^7 different source positions at a redshift of $z_S = 3.0$: bold line: all source positions; thin solid line: singly imaged source positions only; dashed line: multiply imaged source positions only. The top panel displays the differential distribution $f(\mu)$, the bottom panel the integrated one $f(> \mu)$. The typical (unlensed) source becomes slightly fainter, but there is a powerlaw tail of highly magnified but rare sources.

Figure 6 Critical lines in the image plane (Figure 6a) and caustics in the source plane (Figure 6b) for our example line of sight are displayed, for a source redshift of $z_S = 3.0$. The critical lines are the locations at which the determinant of the Jacobian matrix disappears, the caustics are these points, mapped onto the source plane (cf. with Figures 4b and 4a, respectively).

Figure 7 Various image configurations with large magnifications, showing the range of possible geometrical arrangements of images. In the bottom right part of the bottom right panel the size and shape of the unlensed source is indicated (the relative scale is in arcsec).

Figure 8 Various distributions of sources at redshift $z_S = 1.0$ and corresponding images as seen through the three dimensional matter distribution, i.e. weakly and strongly lensed sources. The source configurations are always shown left, the image configurations right. From top to bottom the source ensembles are: circular sources in a regular grid and randomly distributed, and elliptical sources (random orientation) in a regular grid and randomly placed. The source sizes are about 3 arcsec. The source density is equivalent to about 40 000 galaxies per square degree.

Figure 9 Similar to Figure 8, but now source planes (left) and image planes (right) are shown for three different source redshifts. Starting at the top: $z_S = 1$, $z_S = 2$, $z_S = 3$. In the bottom row the superposition of the three source redshifts is shown.

Figure 10 The panels in this figure illustrate the convolution technique as described in the Appendix. In Figure 10a the top left panel represents the matter distribution Σ_1 in one of the $5h^{-1}Mpc$ cubes with average density at redshift $z_L = 0.73$. Here, this particular plane should represent a randomly determined overdensity of 1.6 (a larger than typical case chosen for purpose of illustration); therefore, the matter is contracted in x- and y-direction each by $\sqrt[3]{1.6}$, and multiplied by $\sqrt[3]{1.6}$ (corresponding to a compression in z-direction). The resulting matter distribution is displayed in the top right panel (part of Σ_5 , in the notation of the Appendix). Now, the matter distribution is extended in the “empty” parts of the square, taking advantage of the periodic boundary conditions (lower left panel, full Σ_5). This distribution, now, is shifted in x- and y-direction and rotated by arbitrary amounts, so that finally the lower right panel is obtained (Σ_6). The apparent double appearance of the two dense matter clumps is of no worry, since the bundle of light rays with fixed angular size cuts out only a small square (as indicated in the final panel), so that no repeated structures appear in the “illuminated field”. In Figure 10b the same is shown for a (under-) density of $R = 1.6^{-1} = 0.625$.

Figure 11 Comparison of surface mass density distributions in

$125h^{-1}\text{kpc}\times 125h^{-1}\text{kpc}\times 100h^{-1}\text{Mpc}$ cylinders using the convolution technique (see appendix A; solid histogram) and a direct simulation (Bertschinger 1996; dotted histogram). It indicates that the convolution method gives results which are in satisfactory agreement with direct simulations, where comparisons can be made.

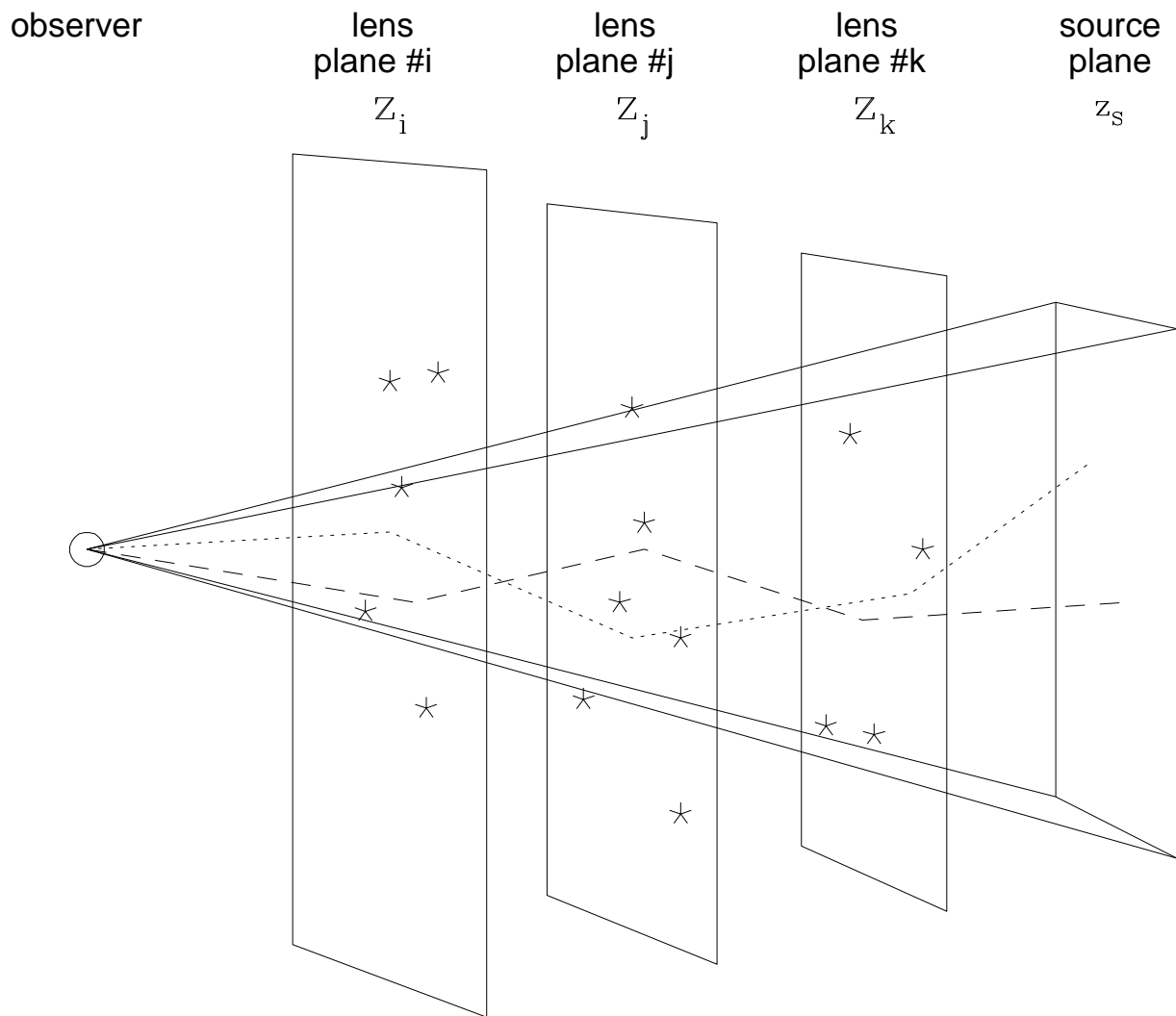


Figure 1

This figure "method_fig2a.gif" is available in "gif" format from:

<http://arXiv.org/ps/astro-ph/9610096v1>

This figure "method_fig2b.gif" is available in "gif" format from:

<http://arXiv.org/ps/astro-ph/9610096v1>

This figure "method_fig3a.jpg" is available in "jpg" format from:

<http://arXiv.org/ps/astro-ph/9610096v1>

This figure "method_fig3b.jpg" is available in "jpg" format from:

<http://arXiv.org/ps/astro-ph/9610096v1>

This figure "method_fig4a.jpg" is available in "jpg" format from:

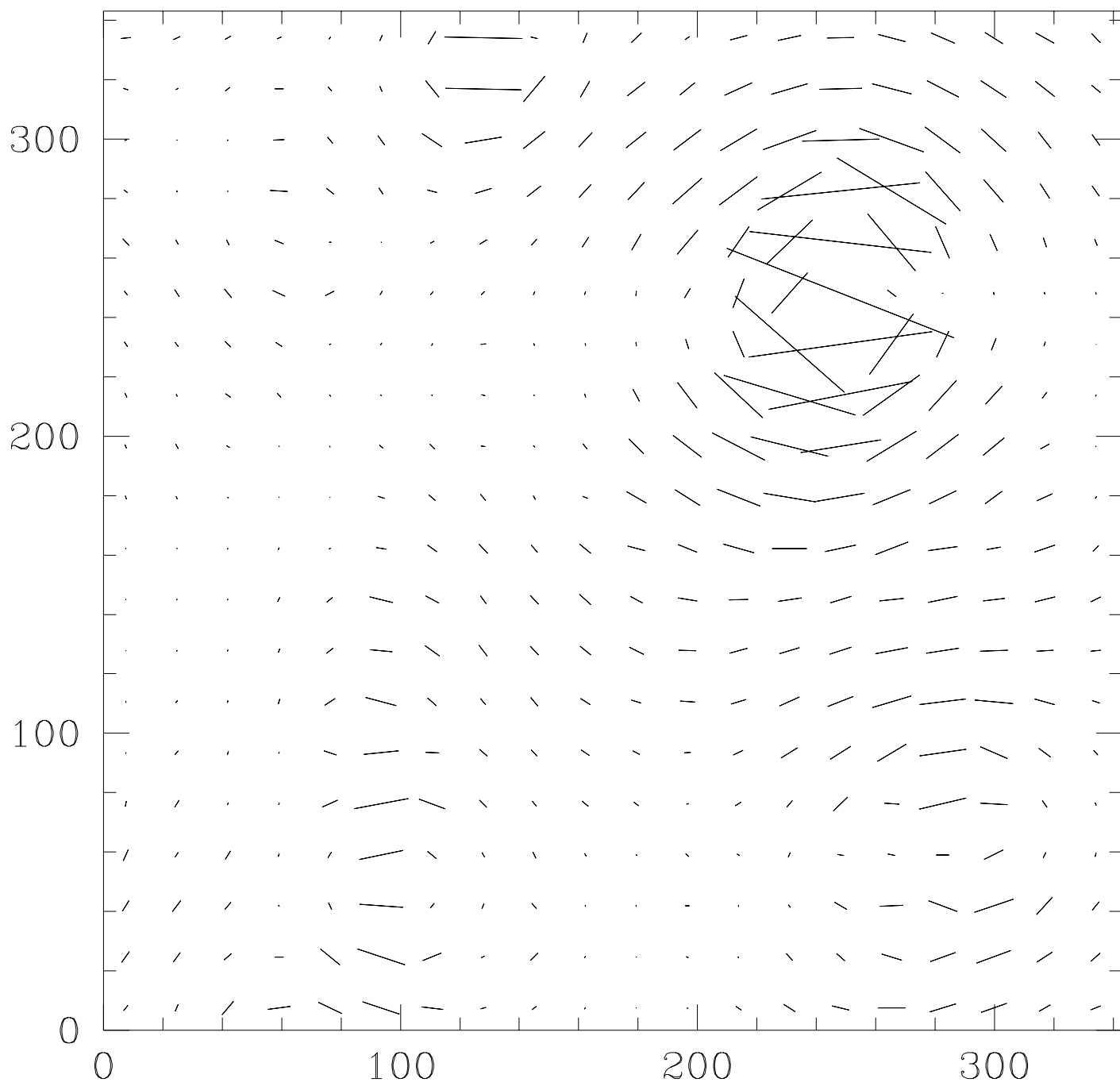
<http://arXiv.org/ps/astro-ph/9610096v1>

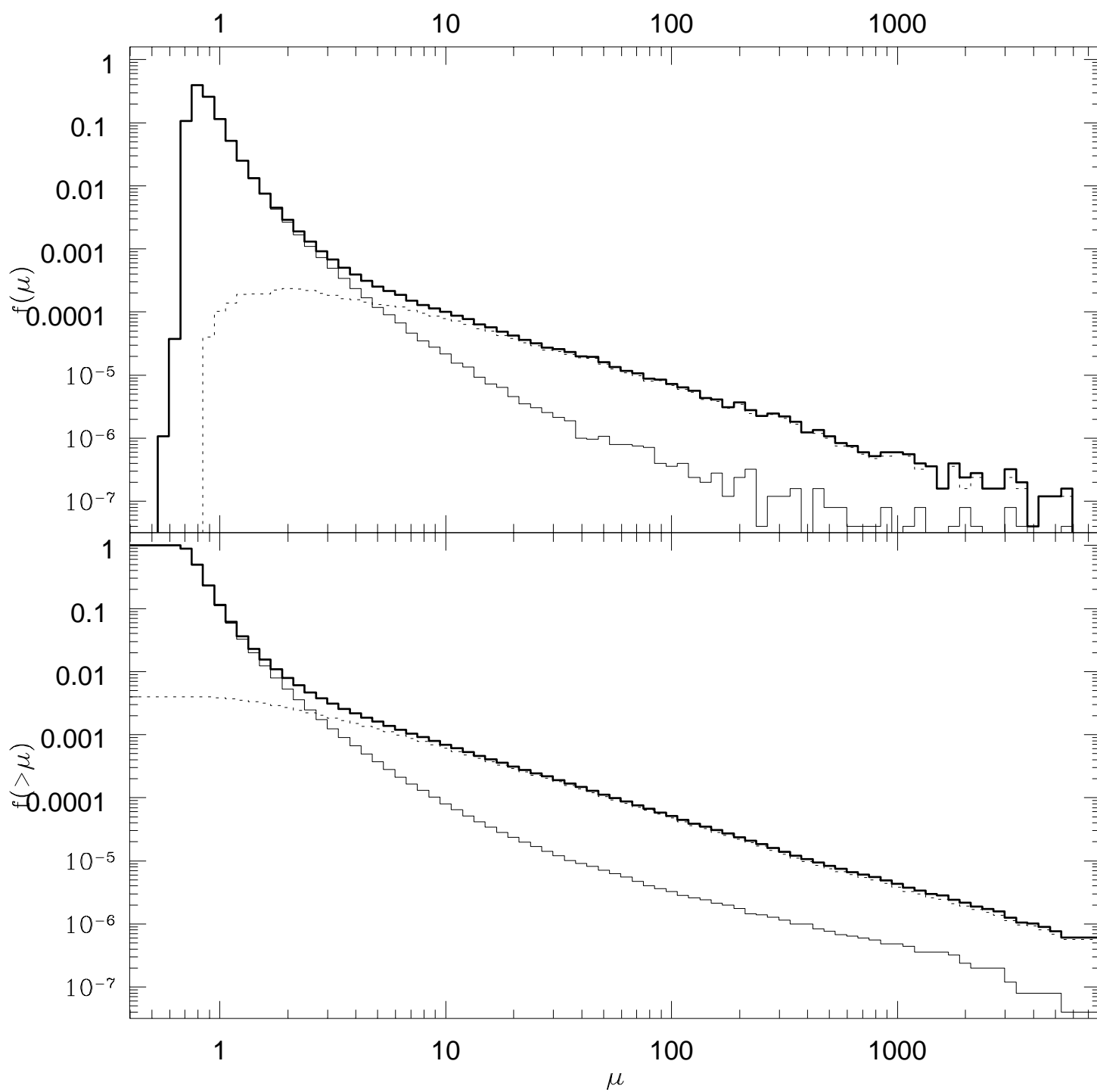
This figure "method_fig4b.jpg" is available in "jpg" format from:

<http://arXiv.org/ps/astro-ph/9610096v1>

This figure "method_fig4c.jpg" is available in "jpg" format from:

<http://arXiv.org/ps/astro-ph/9610096v1>





This figure "method_fig6a.gif" is available in "gif" format from:

<http://arXiv.org/ps/astro-ph/9610096v1>

This figure "method_fig6b.gif" is available in "gif" format from:

<http://arXiv.org/ps/astro-ph/9610096v1>

This figure "method_fig7.gif" is available in "gif" format from:

<http://arXiv.org/ps/astro-ph/9610096v1>

This figure "method_fig8a.gif" is available in "gif" format from:

<http://arXiv.org/ps/astro-ph/9610096v1>

This figure "method_fig8b.gif" is available in "gif" format from:

<http://arXiv.org/ps/astro-ph/9610096v1>

This figure "method_fig8c.gif" is available in "gif" format from:

<http://arXiv.org/ps/astro-ph/9610096v1>

This figure "method_fig8d.gif" is available in "gif" format from:

<http://arXiv.org/ps/astro-ph/9610096v1>

This figure "method_fig9a.gif" is available in "gif" format from:

<http://arXiv.org/ps/astro-ph/9610096v1>

This figure "method_fig9b.gif" is available in "gif" format from:

<http://arXiv.org/ps/astro-ph/9610096v1>

This figure "method_fig9c.gif" is available in "gif" format from:

<http://arXiv.org/ps/astro-ph/9610096v1>

This figure "method_fig9d.gif" is available in "gif" format from:

<http://arXiv.org/ps/astro-ph/9610096v1>

This figure "method_fig10a.jpg" is available in "jpg" format from:

<http://arXiv.org/ps/astro-ph/9610096v1>

This figure "method_fig10b.jpg" is available in "jpg" format from:

<http://arXiv.org/ps/astro-ph/9610096v1>

This figure "method_fig11.gif" is available in "gif" format from:

<http://arXiv.org/ps/astro-ph/9610096v1>